

# Oscillations in a solar filament: first observation of long periods in the He I 584.33 Å line, modelling and diagnostic<sup>\*</sup>

G. Pouget, K. Bocchialini, and J. Solomon

Institut d'Astrophysique Spatiale, CNRS, Université Paris-Sud 11, Bâtiment 121, 91405 Orsay Cedex, France  
e-mail: guillaume.pouget@ias.u-psud.fr

Received 22 July 2005 / Accepted 11 December 2005

## ABSTRACT

Three long observations of filaments were carried out in the 584.33 Å He I line during MEDOC campaigns in November 2003 and November 2004, by the Coronal Diagnostic Spectrometer onboard SOHO. Their duration was 15–16 h and the temporal resolution was 20 s, allowing measurements of the entire range of periodicities theoretically expected in a filament (particularly both the short periods, less than 10 min, and the long ones, more than 40 min). Fourier analysis of the Doppler velocities in the filament allows us to detect oscillations over a wide range, and particularly very slow velocity oscillations (5–6 h) that were not detected previously. We test an earlier interpretation of these velocity oscillations in the prominence model of Joarder & Roberts (1993, A&A, 277, 225), who treat the prominence as a slab. We used a systematic method to identify the six fundamental modes predicted by the model among the numerous frequencies detected. Identification of these modes – and especially the slowest one, the slow kink mode – provides a complete diagnostic of the filament in terms of the Alfvén speed, temperature, and angle between the magnetic field and the main axis of the filament.

**Key words.** Sun: filaments – Sun: prominences – Sun: UV radiation – Sun: oscillations – magnetohydrodynamics (MHD) – waves

## 1. Introduction

Prominence oscillations have been observed for many years (see reviews by Oliver 1999; Oliver & Ballester 2002; Patsourakos & Vial 2002, and the article of Bocchialini et al. 2001). In their introduction Régnier et al. (2001) summarize the main historical steps in both the observational facts and theoretical developments of prominence oscillations. These oscillations are usually classified as short ( $T < 10$  min), intermediate ( $10 \text{ min} < T < 40$  min), and long ( $T > 40$  min).

The MHD models for prominences predict a large variety of oscillation modes. The predicted periods range from a few minutes to a few hours. In particular, in the model proposed by Joarder & Roberts (1992, 1993), which considers the prominence as a whole structure, the slow kink mode (the slowest mode) is expected to have a period on the order of 5 h. Foullon et al. (2004) have reported the detection of long intensity oscillations in a time series of 195 Å EIT images located on a filament, but the observation of such long period velocity oscillations have not been reported in the literature so far.

In this paper, we present and interpret some filament observations carried out during the Medoc (Multi-Experiment Data Operation Center, <http://www.ias.u-psud.fr/medoc/>) campaigns of November 2003 and November 2004. In Sect. 2 we describe our observations, and explain the method followed

to detect the oscillation frequencies with a Fourier analysis. In Sect. 3 we compare the detected frequencies with the frequencies predicted by the model, by using a systematic method that takes into account both the model properties and reasonable ranges for the prominence parameters. The six fundamental modes of the model are identified. From this identification, we deduce a diagnostic of the prominence parameters and found values for the temperature and the angle between the magnetic field lines and the prominence axis, and also a relation between the magnetic field and the square root electron density via the value of the Alfvén speed.

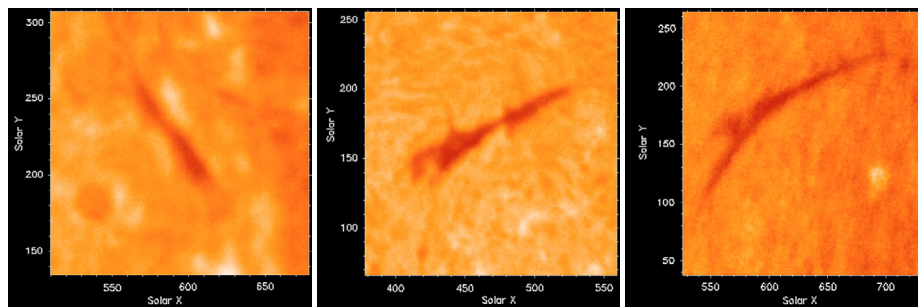
## 2. Observations

During the 12th and 14th Medoc campaigns we obtained long observations of filaments with the coronal diagnostic spectrometer (CDS), one of the EUV spectrometers onboard SOHO (Fleck et al. 1995). The observations were carried out on 22 November 2003 and on 11 and 12 November 2004. The 11 and 12 November observations were both centered on the same filament.

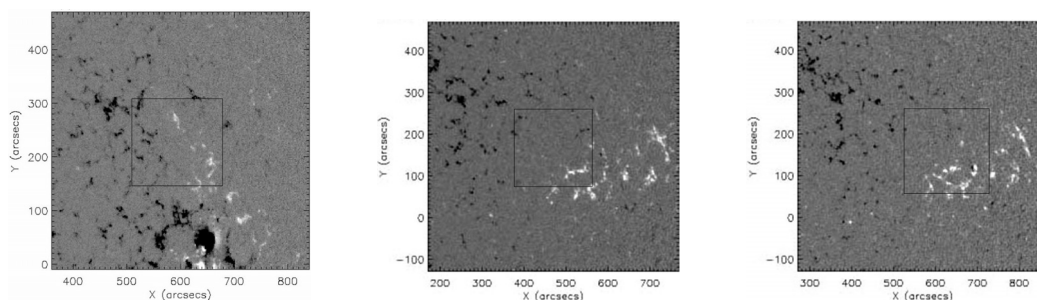
### 2.1. Overview of the observed areas

Figure 1 shows the filaments of the three observations in H $\alpha$  obtained from Big Bear Solar Observatory and Meudon Observatory. Note that the 11 November 2004 filament retained roughly a similar shape on 12 November 2004, although

<sup>\*</sup> Appendix A is only available in electronic form at <http://www.edpsciences.org>



**Fig. 1.** From left to right:  $H\alpha$  images from Big Bear Solar Observatory (BBSO) taken at 17:25 UT on 22 November 2003 and at 17:06 UT on 11 November 2004;  $H\alpha$  image from Meudon Observatory taken at 8:23 UT on 12 November 2004.



**Fig. 2.** From left to right: MDI magnetograms taken on 22 November 2003 (17:35 UT), 11 November 2004 (17:35 UT), 12 November 2004 (7:59 UT). Negative polarities are in black, positive polarities in white. The rectangles represent the areas covered for each day by the corresponding  $H\alpha$  images in Fig. 1.

**Table 1.** Temporal parameters of the observations.

Observation	22 November 2003	11 November 2004	12 November 2004
Name	Fil 1	Fil 2	Fil 3
Beginning (UT)	7:00	5:26	7:15
End (UT)	23:00	20:34	22:23
Duration	16:00	15:08	15:08

its curvature increased. Figure 2 shows magnetograms taken with the Michelson Doppler Imager (MDI) for both filaments. This instrument provides maps of the longitudinal magnetic field strength in the photosphere. On these maps, the filament is located in the channel between the two opposite polarities. The magnetic environment of the filament remains the same on 11 November 2004 and 12 November 2004.

## 2.2. The CDS data sets

Table 1 displays the duration of each observation obtained with the CDS and its dates of beginning and end; Table 2 summarizes the instrumental properties common to the three observations. It is important to note that the temperature of the line observed, HeI 584.33 Å, is 20 000 K, which consequently corresponds to the upper layer of the prominence or to the beginning of the prominence-corona transition region (PCTR). During the analysis of the velocity oscillations in the next sections, we considered that the movements of the prominence core were communicated to the material seen at 20 000 K.

During the three observations, the slit  $X$  position was regularly shifted, in order to compensate for the solar rotation

**Table 2.** Instrumental parameters of the observations.

line	HeI (584.33 Å, 20 000 K)
slit dimensions ( $x \times y$ )	4'' $\times$ 240''
exposure time	15 s
temporal resolution	20 s
spatial resolution along $y$	1.68''

and to follow the same part of the filament from the beginning to the end of the observation. The data sets obtained were 3-dimensional cubes ( $\lambda, y, t$ ), where  $\lambda$  is the wavelength,  $y$  the slit direction – which is 141 pixels high (240'') –, and  $t$  the time. The usual corrections were applied to these data: division by a flatfield, removing of the cosmic rays, correction of some geometric instrumental effects.

A detailed data analysis follows, based on the observation of the 22 November 2003 filament (hereafter Fil 1). The analysis of the observation of the 11 (hereafter Fil 2) and 12 (hereafter Fil 3) November 2004 filament follows in exactly the same way.

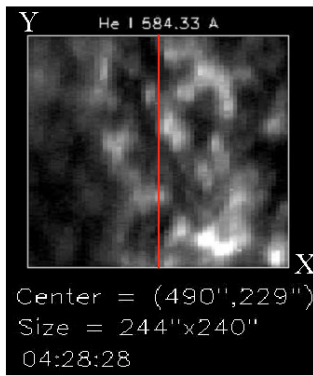


**Fig. 3.** Context view of the filament in HeI obtained with the CDS at 4:28 UT on 22 November 2003 (image centered at  $X = 490''$ ,  $Y = 229''$ ; size =  $244'' \times 240''$ ). The red line represents the CDS slit position.

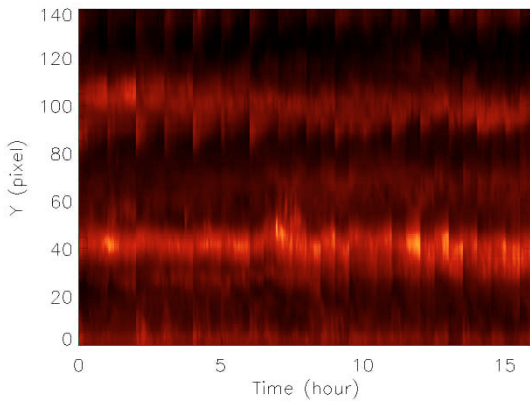


**Fig. 4.** Intensity time series along the slit derived from CDS observations on Fil 1.

### 2.3. Intensity and velocity time series obtained with CDS

Fil 1 is visible on a context view of the filament, taken in HeI just before our observation (Fig. 3). The slit position is plotted in red: the slit cuts the filament near the center of the image. This context view was taken just before our “sit and stare” observation, during which the slit followed the same part of the filament.

By averaging the HeI profiles on the wavelength  $\lambda$  for each time and position  $(t, y)$  of the cube  $(\lambda, y, t)$ , we obtained the integrated intensity time series (Fig. 4). In order to observe the same part of the filament during the whole observation, the solar rotation was compensated for every hour: since this filament is not a horizontal structure, it moves slowly along the  $y$  direction between two compensations for the rotation.

Since the filament is darker than its environment, the filament is located in a minimum of the intensity plotted as a function of  $y$ , for each time position of the intensity time series. The position of this minimum is determined with the help of the context view (Fig. 3), on which it is possible to locate the position of the filament along the slit. For example, Fig. 5 features the intensity (averaged on the wavelength  $\lambda$ ) plotted as

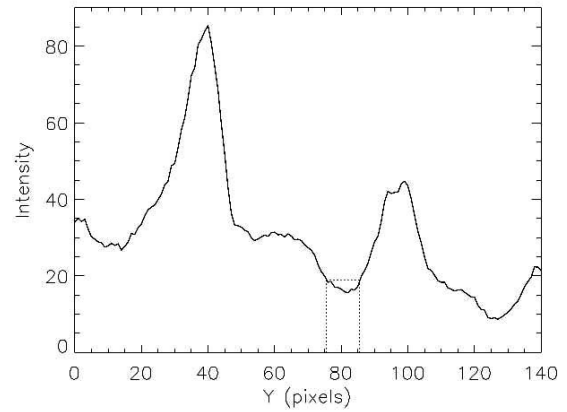


**Fig. 5.** Intensity plotted as a function of  $y$  for a given time position  $t$  of the Fil 1 observation. The threshold retained for this time position corresponds to the horizontal dotted line, while the area detected for the filament is located between the two vertical dotted lines.

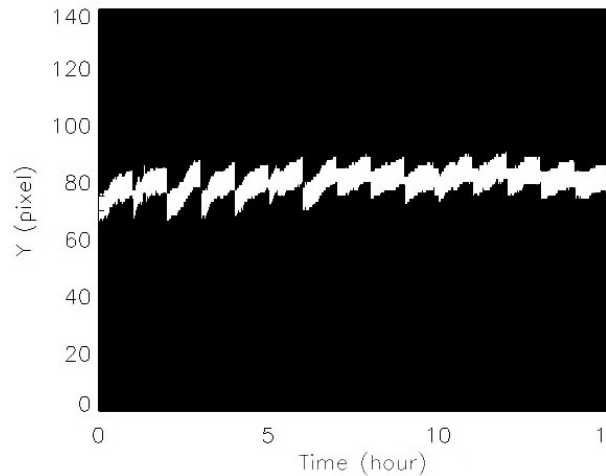


**Fig. 6.** Shape of the filament detected with a threshold along the slit for Fil 1.

a function of  $y$ , for a given time position  $t$ : the minimum corresponding to the filament is located around the position  $y = 80$ . The total width of this minimum is about 20 pixels, i.e. about 34 arcsec (As reported by Heinzel et al. 2001, the EUV filament is larger than the  $H\alpha$  filament, whose width is on the order of 5–10'', see Sect. 3.2.) . In order to analyze only the movements affecting in the filament, we chose to focus on a width of  $34''/2 = 17''$ , centered on this minimum, thereby detecting the core of the minimum, which means the core of the filament.

In order to detect the filament body with this constant width along  $y$  (17'' or 10 pixels), we used the following method. For each time position  $t$ , the pixels  $(t, y)$  that belong to the filament are those of the minimum whose intensity is below a threshold set to an adjustable value, chosen such that the filament width remains equal to 10 pixels for every  $t$ . The result of this detection is plotted with dotted line in Fig. 5. The shape of the part of the filament over the whole observation is plotted in Fig. 6.

We calculated the velocity for each spatial position and time  $(t, y)$  by using the Doppler effect. We took as a reference in the calculation the profile averaged on  $y$  and  $t$  and assumed that

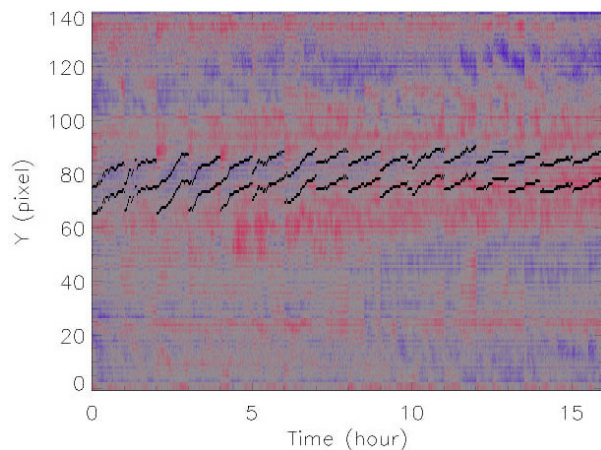


**Fig. 7.** Velocity time series for Fil 1. Blue (red) corresponds to upwards (downwards) motions. The contours of the filament detected are plotted in black.

the velocity averaged on  $y$  and  $t$  is equal to zero. The velocity time series (Fig. 7) were then derived by using a fit routine for each spectral profile in  $(y, t)$  that takes into account the asymmetric shape of the profiles obtained with the CDS after the 1998 recovery (Thompson, CDS note 53, 1999). Over the area of the filament, the absolute amplitude of the velocity variations is about  $15 \text{ km s}^{-1}$ .

In order to analyze the oscillations in the filament, the mean velocity on the width of the filament was then calculated for each temporal sample; thus we obtained a signal  $v = f(t)$ . Figure 8 features the velocities obtained for Fil 1 and also for the two other observations Fil 2 and Fil 3, following exactly the same method as described above.

#### 2.4. Fourier analysis

The frequency analysis was done by computing the Lomb-Scargle periodogram (Scargle 1982) of the signal  $v(t) - \langle v(t) \rangle$  (Fig. 9). We used an algorithm taking into account the fact that the time series were very slightly unevenly sampled, due to a gap of a few seconds between two consecutive blocks of 30 exposures (the time series have 2880 exposures for Fil 1 and 2700 for Fil 2 and Fil 3). The periodogram is calculated without any oversampling, in order to keep the spectral samples statistically independent, which is essential for determining noise thresholds. We consequently evaluated the periodogram every  $\frac{1}{T}$  Hz, with  $T$  the total duration of our observation. The minimal detectable frequency is  $\frac{2}{T} = F_{\min} = 0.0348 \text{ mHz}$  for Fil 1, while the Nyquist frequency is  $25 \text{ mHz}$ .

Our power spectrum exhibits numerous power peaks. Two criteria were applied in order to retain only the significant peaks. First we compare the power spectrum of the filament and the power spectrum of a “reference” area corresponding to the quiet sun (located between  $y = 10$  and  $y = 20$  in Figs. 4 and 7). We eliminated the peaks common to both power spectra (this method eliminates the frequencies artificially introduced by the compensation for the solar rotation).

Second we set a noise threshold. As can be seen in Fig. 9, while the local mean value decreases with frequency in the

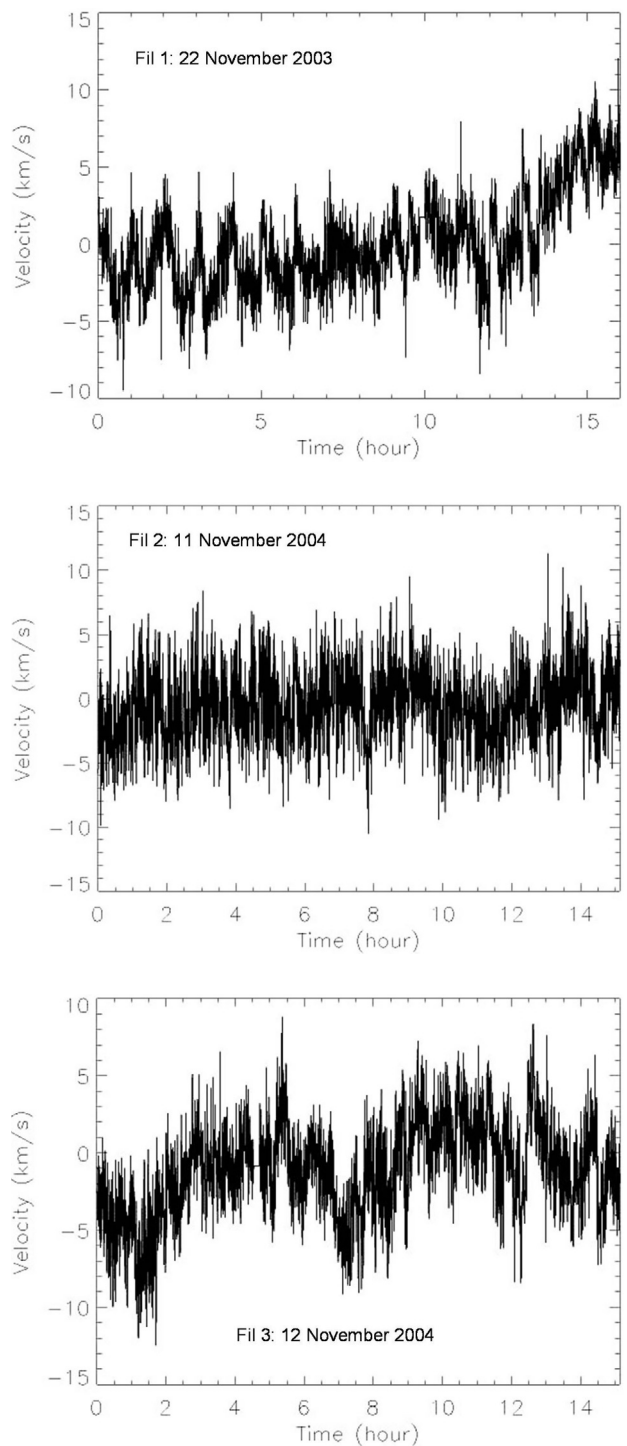


**Fig. 8.** From top to bottom: velocity in the filament as a function of time for Fil 1, Fil 2, and Fil 3.

range  $[0 \text{ mHz}, 3 \text{ mHz}]$  (red noise), it is roughly constant for the range  $[3 \text{ mHz}, 25 \text{ mHz}]$  (white noise). We consequently modeled the background continuum of the spectrum with a Markov red noise added to a constant:

$$P(k) = a + b \frac{1 - \alpha^2}{1 + \alpha^2 - 2\alpha \cos(2\pi k/N)} \quad (1)$$

where  $N$  is the number of exposures,  $k = 0, \dots, N/2$  is the frequency index,  $\alpha$  is the lag-1 autocorrelation coefficient, and

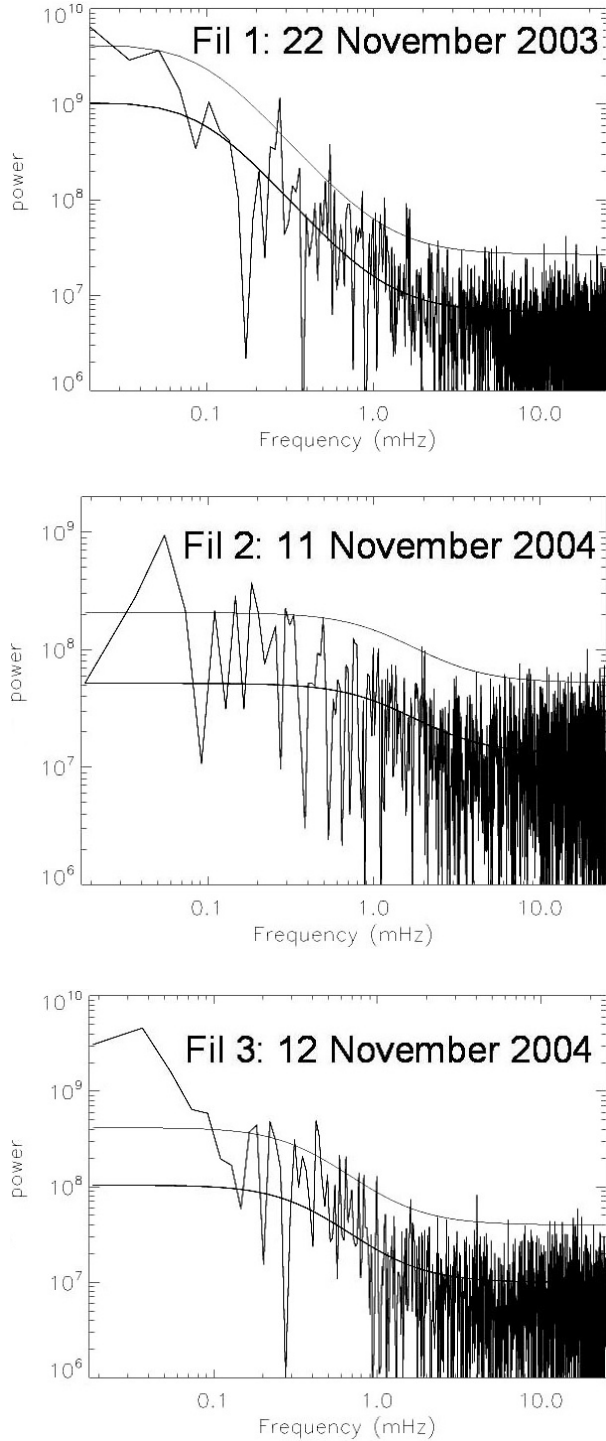


**Fig. 9.** From top to bottom: Lomb-Scargle periodogram of the filament velocity for Fil 1, Fil 2, and Fil 3, plotted with log-log scales. The function fitted to model the null continuum (which is considered as a Markov red noise at low frequencies, typically lower than 3 mHz, and a white noise at high frequencies, typically higher than 3 mHz) is plotted on the same graph; a threshold equal to 4 times this function is set, corresponding to a 98% confidence level for each point of the spectrum.

$a$  and  $b$  are constants. Such a function is fitted to the periodogram by adjusting the  $\alpha$ ,  $a$ , and  $b$  parameters, and a threshold equal to four times this function is set (Fig. 9), which means

**Table 3.** Frequencies detected (mHz) in the 3 data sets Fil 1, Fil 2, and Fil 3.

Frequency number	Fil 1	Fil 2	Fil 3
$f_1$	0.0516	0.0532	0.0441
$f_2$	0.275	0.147	0.184
$f_3$	0.860	0.184	0.24
$f_4$	1.17	0.293	0.42
$f_5$	1.62	0.330	0.44
$f_6$	1.65	0.496	0.59
$f_7$	2.17	1.95	0.64
$f_8$	2.44	2.02	0.99
$f_9$	4.68	4.13	1.60
$f_{10}$	5.14	6.15	2.33
$f_{11}$	5.47	7.53	2.64
$f_{12}$	10.61	8.37	4.06
$f_{13}$	14.32	8.63	6.30
$f_{14}$	16.37	8.79	7.95
$f_{15}$	16.49	10.96	11.35
$f_{16}$	21.92	11.34	12.08
$f_{17}$	22.22	12.89	13.47
$f_{18}$		14.74	15.70
$f_{19}$		15.44	15.94
$f_{20}$		17.49	16.80
$f_{21}$		18.82	17.62
$f_{22}$		19.29	20.91
$f_{23}$		20.98	
$f_{24}$		21.26	
$f_{25}$		22.89	
$f_{26}$		23.86	
$f_{27}$		24.49	

a 98% confidence level for each point of the spectrum (Horne et al. 1985); the validity and the significance of such a threshold are tested in Sect. 3.3, where Monte-Carlo simulations are made in order to determine the false alarm probability of our whole diagnostic process. We retained only the power peaks above this threshold. The same method was applied for Fil 2 and Fil 3.

See Appendix A for the detailed power spectra of each observation.

The first striking result is the detection of long periods for each observation. To more accurately determine the values of these low frequencies, we plotted the 10 times oversampled periodograms (Fig. 10): the periods are 5.4 h (0.0516 mHz) for Fil 1, 5.2 h (0.0532 mHz) for Fil 2, and 6.3 h (0.0441 mHz) for Fil 3. Such long periods of several hours are predicted by the model of Joarder and Roberts, but have not been observed previously. Their detection allows us to do a complete diagnostic of the observed filaments (Sect. 3).

Table 3 shows the frequencies retained with this method for the three observations. Seventeen frequencies were identified for Fil 1, ranging from 0.0516 mHz to 22.22 mHz. Twenty-seven frequencies are identified for Fil 2, and twenty-two for Fil 3.

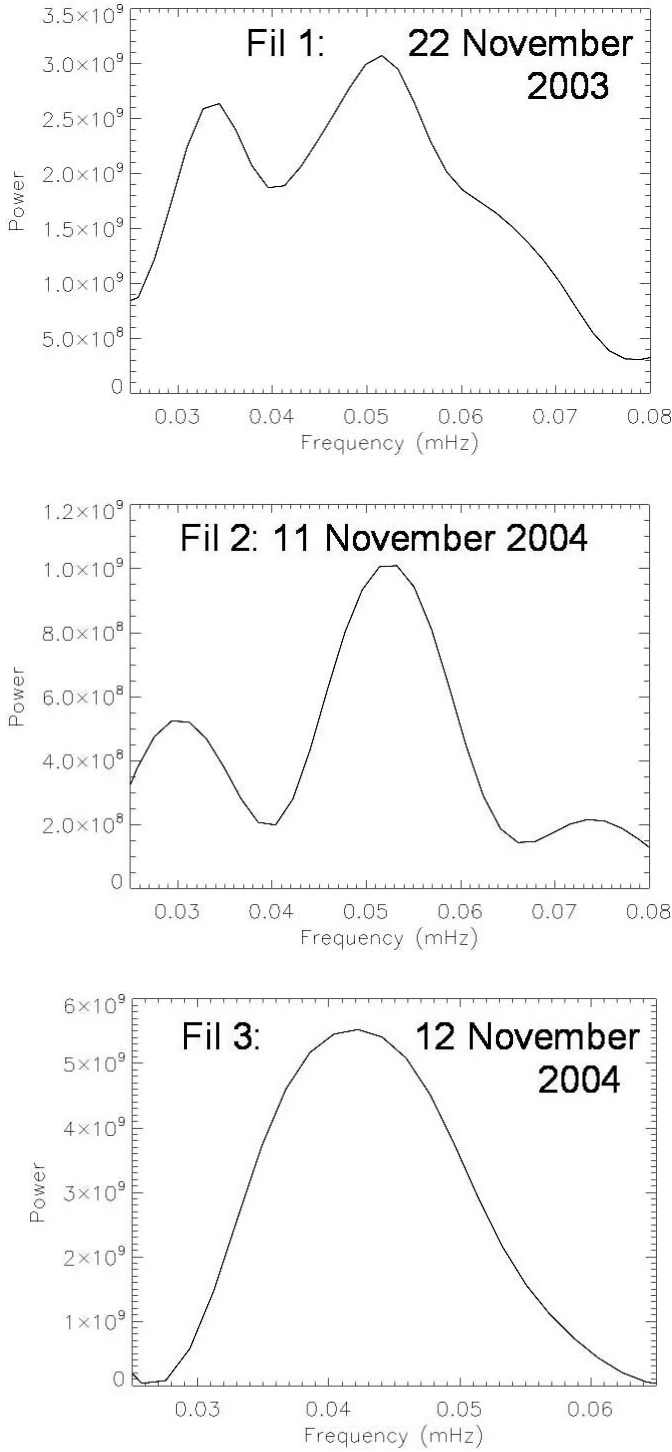


**Fig. 10.** From top to bottom: 10 times oversampled periodograms of the filament velocity for Fil 1, Fil 2, and Fil 3, on a range covering the lowest power peak for each observation. These oversampled periodograms are plotted to determine the frequency value of this peak accurately.

### 3. Comparison with a model

#### 3.1. Model

We used the prominence model of Joarder & Roberts (1993), which takes the global modes of oscillation of the prominence

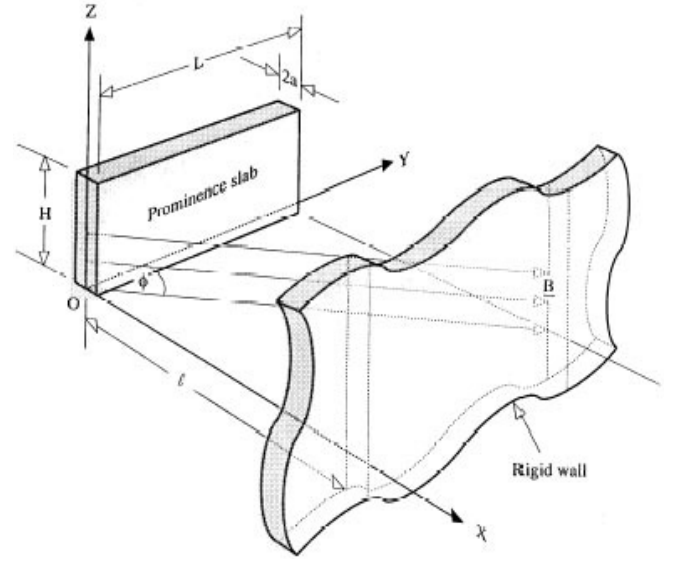


**Fig. 11.** Diagram of the prominence and its environment in the Joarder & Roberts model (1993).

into account. We did not consider models that examine the prominence fine structures (the models of Joarder et al. 1997 and Diaz et al. 2003 consider the prominence as a group of small-scale fibrils), because the resolution with the CDS is not sufficient to detect them: the typical width of a fibril is less than 500 km, while the spatial resolution with the CDS is  $1.68 \times 730 \text{ km} = 1230 \text{ km}$ . By averaging the velocity along the  $y$  dimension, we considered the filament as a whole structure.

In this model (Fig. 11), the filament is described as a slab (width =  $2a$ ) embedded in a uniform magnetic field (its value  $B$  is the same in the prominence and its environment). The field line curvature is ignored, and the magnetic field makes an angle  $\phi$  to the long axis of the slab. In order to represent the photospheric line-tying effect, the field lines are tied to rigid walls (which are perfect conductors) at  $x = \pm l$  on either side of the slab. Gravity is ignored. The slab is defined by a constant density ( $\rho = m_{H^+} n_{H^+} = m_{H^+} n_e$ , with  $n_e$  the electronic density,  $n_{H^+}$  the proton density) and temperature ( $T$ ), which are different from those of the surrounding corona.

The dispersion relations lead to 6 fundamental modes, whose frequencies are called primary frequencies, that can be classified into 3 pairs, each pair having the same phase speed (Régnier et al. 2001). Even and odd Alfvén modes ( $eam$  &  $oam$ ), “kink” and “sausage” slow magnetoacoustic modes ( $skm$  &  $ssm$ ), “kink” and “sausage” fast magnetoacoustic modes ( $fkm$  &  $fsm$ );  $eam$ ,  $skm$  and  $fkm$  are called even modes, while  $oam$ ,  $ssm$  and  $fsm$  are called odd modes.

The primary frequencies are functions of the different prominence parameters. Conversely these parameters, namely the angle  $\phi$ , the speed of sound  $c_s = \sqrt{\frac{\gamma k_B T}{m_{H^+}}}$ , and the Alfvén speed  $v_A = \frac{B}{\sqrt{\mu_0 \rho}}$ , can be expressed as a function of the primary frequencies (Régnier 2001):

$$\sin(\phi) = \frac{f_{oAm}^2}{\sqrt{f_{ssm}^2 (f_{oAm}^2 - f_{fsm}^2) + f_{oAm}^2 f_{fsm}^2}} \quad (2)$$

**Table 4.** Frequencies and periods of the six fundamental modes obtained for the three observations Fil 1, Fil 2, and Fil 3.

Mode	Fil 1: 22/11/2003	Fil 2: 11/11/2004	Fil 3: 12/11/2004
<i>skm</i>	0.0516 mHz/5.4 h	0.0532 mHz/5.2 h	0.0441 mHz/6.3 h
<i>ssm</i>	0.28 mHz/1 h	0.29 mHz/57 min	0.24 mHz/70 min
<i>eAm</i>	0.86 mHz/19 min	2 mHz/8.3 min	2.3 mHz/7.2 min
<i>oAm</i>	4.7 mHz/3.6 min	11.3 mHz/1.5 min	12.1 mHz/1.4 min
<i>fkm</i>	2.4 mHz/6.8 min	4.1 mHz/4 min	4.1 mHz/4.21 min
<i>fsm</i>	14.3 mHz/1.2 min	21 mHz/0.8 min	20.9 mHz/0.8 min

**Table 5.** Values obtained for the prominence parameters for the three observations. Note that the last two rows only show some estimations for  $B$  and  $n_e$ , by supposing a value for, respectively,  $n_e$  and  $B$ : the complete diagnostic provides values of  $\phi$ ,  $T$ , and  $v_A$ .

Parameter	Fil 1: 22/11/2003	Fil 2: 11/11/2004	Fil 3: 12/11/2004
$\eta$ value retained	0.18	0.19	0.19
$\phi$	19°	33°	35°
$T$	6200 K	11 700 K	6800 K
$B/\sqrt{n_e}$	$7.2 \times 10^{-5}$	$22.5 \times 10^{-5}$	$22.4 \times 10^{-5}$
$v_A = B/\sqrt{\mu_0 n_e m_p}$	157 km s <sup>-1</sup>	490 km s <sup>-1</sup>	488 km s <sup>-1</sup>
$n_e$ ( $B = 10$ G)	$1.9 \times 10^{10}$ cm <sup>-3</sup>	$2 \times 10^9$ cm <sup>-3</sup>	$2 \times 10^9$ cm <sup>-3</sup>
$B$ ( $n_e = 2 \times 10^{10}$ cm <sup>-3</sup> )	10.2 G	32 G	31.7 G

$$c_s = \frac{4a f_{ssm} f_{fsm}}{f_{oAm}} \quad (3)$$

$$v_A = \frac{4a}{f_{oAm}} \sqrt{f_{ssm}^2 (f_{oAm}^2 - f_{fsm}^2) + f_{oAm}^2 f_{fsm}^2}. \quad (4)$$

If we determine the values of the primary frequencies, these three equations give us the angle  $\phi$ , the temperature  $T$ , and a relation between  $B$  and  $n_e$ . Thus the knowledge of the primary frequencies leads to a diagnostic of the prominence.

With the frequencies that we have detected (Sect. 2.3), the next step towards a diagnostic is consequently to assign a detected frequency to each fundamental mode. We use the following property in the next paragraphs. The ratio of the primary frequency of the even modes to the primary frequency of the corresponding odd modes ratio only depends on the geometrical parameters  $a$  and  $l$  (Régnier et al. 2001):

$$\frac{f_{eAm}}{f_{oAm}} = \frac{f_{skm}}{f_{ssm}} = \frac{f_{fkm}}{f_{fsm}} = \frac{2}{\pi} \left( \frac{a}{l} \right)^{\frac{1}{2}} = \eta. \quad (5)$$

Note that following Joarder & Roberts (1993), the above formulae (1)–(4) result from the approximate dispersion relations obtained in the limit of infinite wavelength in the  $y$  and  $z$  direction (i.e.  $k_y = k_z = 0$ ). Nevertheless, a numerical solution of the exact dispersion relation shows that, at least for the six fundamental modes that we consider, the frequencies obtained are not dramatically sensitive to the value of the parameter  $\kappa l = (k_y^2 + k_z^2)l$  (see Fig. 2 of Joarder & Roberts 1993).

Another important point is that the dominant velocities of the six modes have different polarizations: the compressive modes (*skm*, *ssm*, *fkm*, *fsm*) have dominant velocities oriented in the direction of propagation, while Alfvén modes (*eAm*, *oAm*) have velocities orthogonal to this direction. Up to now the dominant polarization of the modes in this model has not been obtained and the measurement of these polarizations is beyond the current observational capacities. In our data analysis, we admit that we are not watching in any particular direction with

respect to the wave propagation directions and that we are observing velocity projections of the whole modes on the line of sight.

The first step towards the diagnostic is to determine these two parameters  $a$  and  $l$ , in order to obtain  $\eta$ . As for the preceding analysis, the detailed method to obtain the diagnostic is only presented for Fil 1, and a synthesis of the results is presented for the three observations in Tables 4 and 5.

### 3.2. Determination of the parameters $a$ and $l$

In order to avoid the geometrical projection effects, we measured  $a$  on an H $\alpha$  image taken 4 days earlier (18 November 2003), when the filament was near the disk center (Fig. 12). We obtained the following range for  $2a$ :  $3600 \text{ km} < 2a < 7300 \text{ km}$ . We retained a mean value  $a = 2700 \text{ km}$ . For Fil 2 and Fil 3 the value for  $a$  is  $5800 \text{ km} \pm 30\%$ ; we take the same parameter values for 11 and 12 Nov. 2004, because the filament maintains roughly the same shape during the two days.

For the length  $2l$  of the field lines, we used an MDI magnetogram (22 November 2003, Fig. 13). The rigid walls of opposite magnetic polarities are represented by the white and black areas on both sides of the filament. On the magnetogram we measured the value of  $2r$  (Fig. 13) that we corrected for geometrical projection effects. This correction is schematized in Fig. 14. On the 22 November 2003 magnetogram we measured the  $X$  and  $Y$  coordinates of the two points located at both extremities of the arrow: these two points correspond to  $M_1(X_1, Y_1)$  and  $M_2(X_2, Y_2)$  on this diagram. The  $Z$  coordinate of both points is then calculated using spherical coordinates, thereby obtaining the two points  $M'_1(X_1, Y_1, Z_1)$  and  $M'_2(X_2, Y_2, Z_2)$ . The distance between  $M'_1$  and  $M'_2$  gives us  $2r'$ , the corrected value of  $2r$  (the curvature of the sun is neglected).

Then we assume that the field lines are approximately semi-circular, in agreement with theoretical modelling of such stable magnetic structures (Fig. 15). In this configuration we deduce  $l$

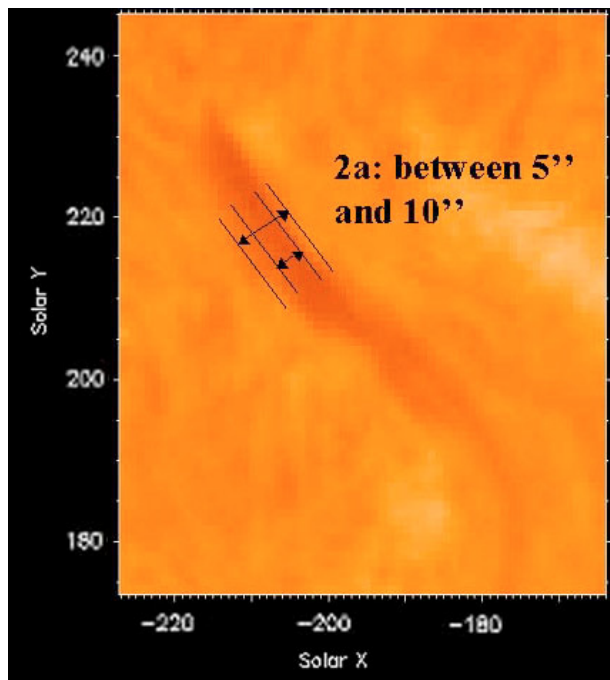


**Fig. 12.**  $H\alpha$  image from the Big Bear Solar Observatory taken on November 18, 2003, showing Fil 1 near the disk center.

from  $l = \frac{\pi}{2}r'$ . We finally obtain  $l = 45\,000$  km ( $\pm 20\%$ ) for Fil 1 ( $l = 57\,000$  km ( $\pm 20\%$ ) for Fil 2 and Fil 3).

### 3.3. Diagnostic

From the values obtained for  $a$  and  $l$ , we deduced an  $\eta$  value of 0.15. Considering the relative uncertainties on  $a$  (70%) and  $l$  (40%), we deduced that the  $\eta$  uncertainty is approximately 50%:  $0.11 < \eta < 0.19$  ( $0.16 < \eta < 0.24$  for 11 and 12 Nov. 2004).

For the diagnostic, we adopted the following method. With the aim of finding the 6 fundamental frequencies of the model, we supposed that we were able to observe all the oscillation modes in our 16-h observation, since the slowest mode is expected at a period of 5 h with standard parameters for the prominence (Joarder & Roberts 1993; Régnier et al. 2001). Our approach was a systematic one, because we allocated every possible triplet of measured frequencies to the 3 odd primary frequencies ( $oam$ ,  $ssm$ ,  $fsm$ ) and then verified the coherence of each choice through successive tests. For each test, if the test was negative, we changed the triplet and started the series of tests again. The 2 successive tests were:

1. For the three frequencies selected, supposed to be the odd frequencies, we searched for – considering Eq. (5) – whether we could find three corresponding even frequencies, with the condition that the ratio of each even frequency by the odd frequency is in the range  $0.11 < \eta < 0.19$ . The differences between the three ratios had also to be lower than 0.02, a value that appeared reasonably small.
2. We then deduced the physical parameters (density ( $n_e$ ), angle ( $\phi$ ), magnetic field ( $B$ ), temperature ( $T$ ), as defined in Eqs. (2)–(4)) of the set of six primary frequencies

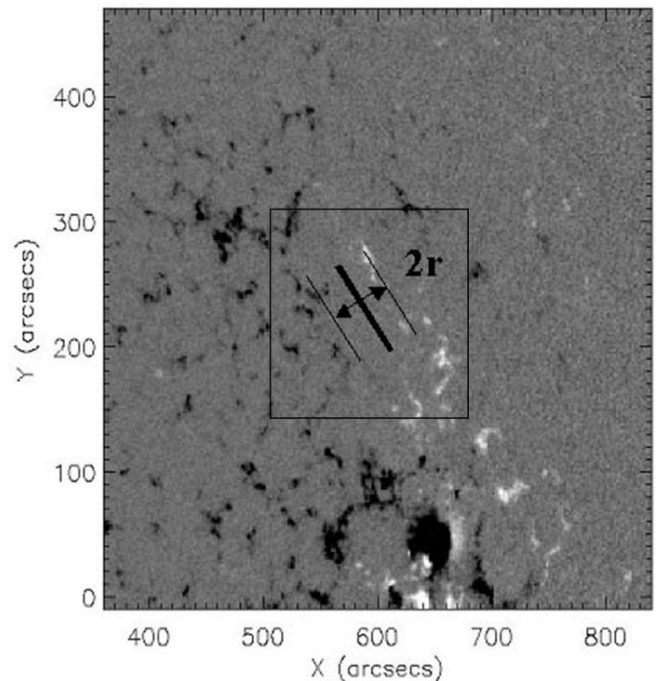


**Fig. 13.** MDI magnetogram taken on November 22, 2003, showing the feet of the magnetic field lines sustaining Fil 1. The field of view is the same as on the magnetogram for Fil 1 in Fig. 2.

satisfying tests 1 and 2. Their values had to be in the following ranges:

- $0^\circ < \phi < 55^\circ$  (Ashbourn et al. 2002);
- $5000 \text{ K} < T < 12\,000 \text{ K}$  (Ofman et al. 1998; Hirayama et al. 1985, both cited in a review by Patsourakos & Vial 2002);
- $1.3 \times 10^9 \text{ cm}^{-3} < n_e (B = 10 \text{ G}) < 3 \times 10^{11} \text{ cm}^{-3}$  (Wiik et al. 1997; Madjarska et al. 1999, both cited by Patsourakos & Vial 2002);
- $B (n_e = 2 \times 10^{10} \text{ cm}^{-3}) > 1 \text{ G}$  (Paletou et al. 2001; Ashbourn et al. 2002; Bommier et al. 1994; Leroy et al. 1983, 1984).

If these 2 tests are satisfied, we considered that we have found all the 6 primary frequencies.

This diagnostic method took as its initial hypothesis that the six oscillation modes are all present in the data. To check the validity of such a method and to establish the conditions of its application, we did a large number of Monte Carlo simulations. Ten thousand data sets of 2700 points (same conditions as for Fil 2 and Fil 3) were generated from a Gaussian distribution; the calculation of the corresponding periodograms led to 10 000 white noise spectra. Then a threshold equal to four times the mean value of the spectra was set, which corresponded to the same confidence level as the one used in Sect. 2.4 (98% confidence level for each point of the spectra). For each spectrum, the set of frequencies detected (usually about 25 frequencies) was injected into our diagnostic method: we supposed that the six modes were present in the set, and we tested if we were able to find them.

Only 4.5% of the simulated spectra gave positive results with our diagnostic method, which gave a “false alarm

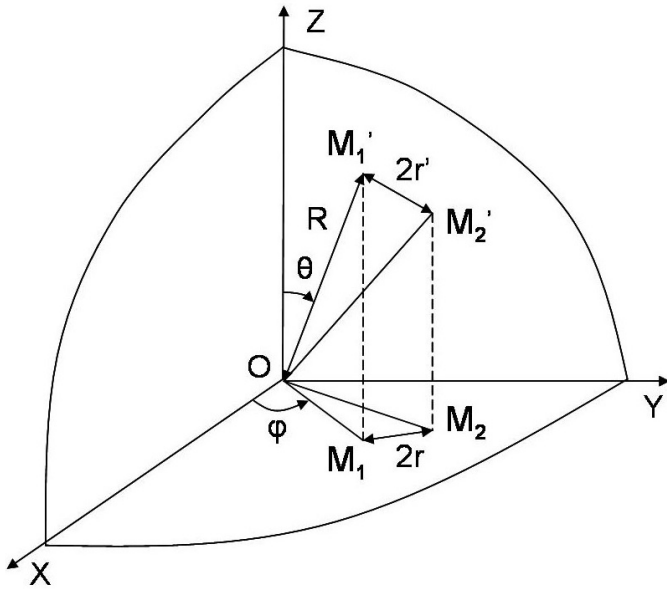


**Fig. 14.** Correction of the geometrical projection effects for  $2r$ , by using spherical coordinates.  $X$  and  $Y$  are cartesian coordinates of the sun seen by SOHO (the origin  $O$  is the center of the sun), and  $Z$  is the axis orthogonal to  $X$  and  $Y$ , pointing towards SOHO.  $R$  is the solar radius.

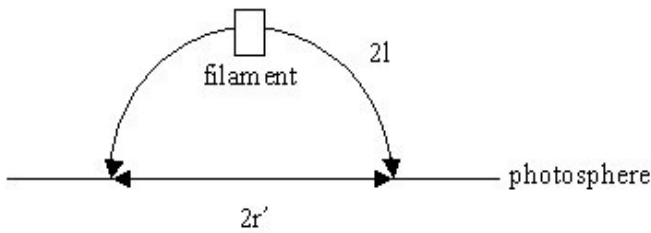


**Fig. 15.** Diagram of a field line. We consider circular field lines:  $2r'$  is the length measured on the MDI magnetogram, while  $2l$  is the real length of the field lines.

probability” for the whole method. This probability is small but not negligible. It allowed us to define the domain of application of the method: one successful diagnostic based on frequencies coming from noise has a 4.5% chance of occurring. In the case of Fil 1, Fil 2 and Fil 3, as it is developed below, the three observations led to three coherent diagnostics, which had 0.009% chances to happen with pure noise: we are consequently confident that our results are based on real, “physical” frequencies.

These three observations led to coherent diagnostics. A single possible set of frequencies was found for each observation. Table 4 displays the results for the primary frequencies for Fil 1, Fil 2, and Fil 3, while Table 5 displays those for the prominence parameters. Note that it is tricky to give uncertainties on the values found for the frequencies and the parameters. The uncertainties on  $a$  and  $l$  are used to calculate the uncertainty of the  $\eta$  parameter but, considering the method followed for the diagnostic, this uncertainty does not give the values of error bars of the frequencies and the parameters but instead introduces some uncertainty into all the diagnostic(s) found. However, for a given diagnostic, the uncertainty of each frequency value is considered equal to  $\frac{1}{2T}$  ( $T$  the total duration of the observation), which means about 0.009 mHz for the three

observations. The corresponding relative uncertainty decreases with increasing frequencies.

The interest of such a diagnostic is to simultaneously determine the values of  $\phi$ ,  $T$ , and the Alfvén speed  $v_A$ , for the same prominence.

This diagnostic shows that the slowest oscillations detected (5.4 h, 5.3 h, and 6.3 h) can be interpreted in terms of slow kink mode. The other modes are found at lower periods that correspond to the short period range (for *fsm*, *oam*, *fk*), the intermediate period range (for *eam*), and the long period range (for *ssm*); see introduction for the corresponding ranges.

The values found for  $\phi$  ( $19^\circ$ ,  $32^\circ$ ,  $35^\circ$ ) are not far from the mean value of  $25^\circ$  observed in quiescent prominences (Leroy et al. 1983, 1984); and it is consistent with the fact that the two prominences observed were quiescent. The Alfvén speeds are high in the range [ $150 \text{ km s}^{-1}$ ,  $500 \text{ km s}^{-1}$ ]. These high values could be explained by the fact that the density is small, which could lead to an increase in  $v_A$ , which is proportional to the inverse of the square root of the density (Sect. 3.1). The temperatures found are scattered and in the range [ $6000 \text{ K}$ ,  $7000 \text{ K}$ ] for Fil 1 and Fil 3; for Fil 2, the temperature ( $11\,700 \text{ K}$ ) is much higher.

The diagnostics obtained for Fil 2 and Fil 3 (the filament is the same for the two observations) are not very different, apart for the temperature values, where  $\phi$  has almost the same value for the two observations ( $32^\circ$  and  $35^\circ$ ) and the Alfvén speed is also the same ( $490 \text{ km s}^{-1}$  and  $488 \text{ km s}^{-1}$ ). But the temperature almost doubles, from  $6800 \text{ K}$  to  $11\,700 \text{ K}$ . The temperature increase seems to indicate a change of state of the filament from one day to the next; but on the other hand, the filament seems to remain in the same geometrical state ( $\phi$  remains the same), and the Alfvén speed does not change. It would be useful in the future to do other continuous long observations of filaments – similar to those presented here – including independent measures of the prominence temperature and density. It would thus be possible to verify the diagnostic found with the oscillation frequencies and to check the validity of the model.

## 4. Conclusions

Three observations were carried out on filaments with CDS/SOHO in 2003 and 2004, using the  $584.33 \text{ \AA}$  HeI line, with a very long duration (15–16 h) and a short time resolution (20 s). These temporal characteristics allowed us to detect both short and long velocity oscillations. We particularly detected very long periodicities, which were not detected previously, ranging from 5 h to 6 h, in each of these observations. We used the Joarder & Roberts model (1993) to interpret these oscillations in terms of Alfvén and magnetoacoustic waves. The six fundamental modes predicted by the model were detected for each observation. In particular the 5–6 h oscillations were interpreted as an effect of the slow kink mode. From the frequencies found for the six modes we derived a complete diagnostic of the filament, in terms of the Alfvén speed, temperature, and angle between the magnetic field and the main axis of the filament. The values found for the angle are, in the three cases, close to the mean value of  $25^\circ$  usually observed in the quiescent prominences. The temperature values are more scattered

(6800 K–11 700 K), while the values of the Alfvén speed are in the range [ $150 \text{ km s}^{-1}$ ,  $500 \text{ km s}^{-1}$ ].

The study of the prominence oscillations also offers perspectives in the domain of CME prediction (and consequently for the space weather), since most of the CMEs occur after a filament eruption – 94% according Zhou et al. (2003). The oscillations could move the prominence into an unstable state, causing its eruption. But the characteristics (frequency range, amplitude, duration) of oscillations capable of provoking an eruption have to be determined, and the way such oscillations occur and induce an unstable state has to be understood.

*Acknowledgements.* SOHO is a mission of international cooperation between ESA and NASA. CDS/SOHO, EIT/SOHO, and MDI/SOHO data have been used courtesy of the CDS, EIT and MDI consortia. The authors are indebted to the BBSO and Meudon Observatory teams for providing the data used here. We would like to thank the MEDOC team at the Institut d’Astrophysique Spatiale for its help in obtaining the CDS data presented in this paper. The authors would like to thank the referee for his constructive remarks. The authors also thank Thierry Appourchaux, Frédéric Auchère, Frédéric Baudin, John Leibacher, Philippe Lemaire, and Jean-Claude Vial for fruitful discussions on the signal analysis methods.

## References

- Ashbourn, J. M. A., & Woods, L. C. 2002, *ApJ*, 568, 1049
- Bocchialini, K., Costa, A., Domenech, G., et al. 2001, *Sol. Phys.*, 199, 133
- Bommier, V., Degl’Innocenti, E. G., Leroy, J. L., et al. 1994, *Sol. Phys.*, 154, 231
- Diaz, A. J., Oliver, R., & Ballester, J. L. 2003, *A&A*, 402, 781
- Fleck, B., Domingo, V., & Poland, A. I. 1995, *The SOHO mission* (Dordrecht: KAP)
- Foullon, C., Verwichte, E., & Nakariakov, V. M. 2004, *A&A*, 427, L5
- Heinzel, P., Schmieder, B., & Tziotziou, K. 2001, *ApJ*, 561, L223
- Hirayama, T. 1985, *Sol. Phys.*, 100, 415
- Horne, J. H., & Baliunas, S. L. 1985, *ApJ*, 302, 757
- Joarder, P. S., & Roberts, B. 1992a, *A&A*, 256, 264
- Joarder, P. S., & Roberts, B. 1992b, *A&A*, 261, 625
- Joarder, P. S., & Roberts, B. 1993, *A&A*, 277, 225
- Joarder, P. S., Nakariakov, V. M., & Roberts, B. 1997, *Sol. Phys.*, 173, 81
- Leroy, J. L., Bommier, V., & Sahal-Brechot, S. 1983, *Sol. Phys.*, 83, 135
- Leroy, J. L., Bommier, V., & Sahal-Brechot, S. 1984, *Sol. Phys.*, 131, 33
- Madjarska, M. S., Vial, J. C., Bocchialini, K., et al. 1999, *Proc. of the 8th SOHO Workshop*, ESA SP-446, 467
- Ofman, L., Kucera, T. A., Mouradian, Z., et al. 1998, *Sol. Phys.*, 183, 97
- Oliver, R., & Ballester, J. L. 2002, *Sol. Phys.*, 206, 45
- Paletou, F., Lopez Ariste, A., Bommier, V., et al. 2001, *A&A*, 375, L39
- Patsourakos, S., & Vial, J. C. 2002, *Sol. Phys.*, 208, 253
- Régnier, S., Solomon, J., & Vial, J. C. 2001, *A&A*, 376, 292
- Régnier, S. 2001, *Ph.D. Thesis*
- Scargle, J. D. 1982, *ApJ*, 263, 835
- Wiik, J. E., Schmieder, B., Kucera, T., et al. 1997, *Sol. Phys.*, 187, 405
- Zhou, G., Wang, J., & Cao, Z. 2003, *A&A*, 397, 1057

# Online Material

## **Appendix A: Power spectra**

In Figs. A.1–A.3 the power spectra are displayed of the observed filaments (continuous line) and of the corresponding reference areas (dotted line) for the different frequency ranges.

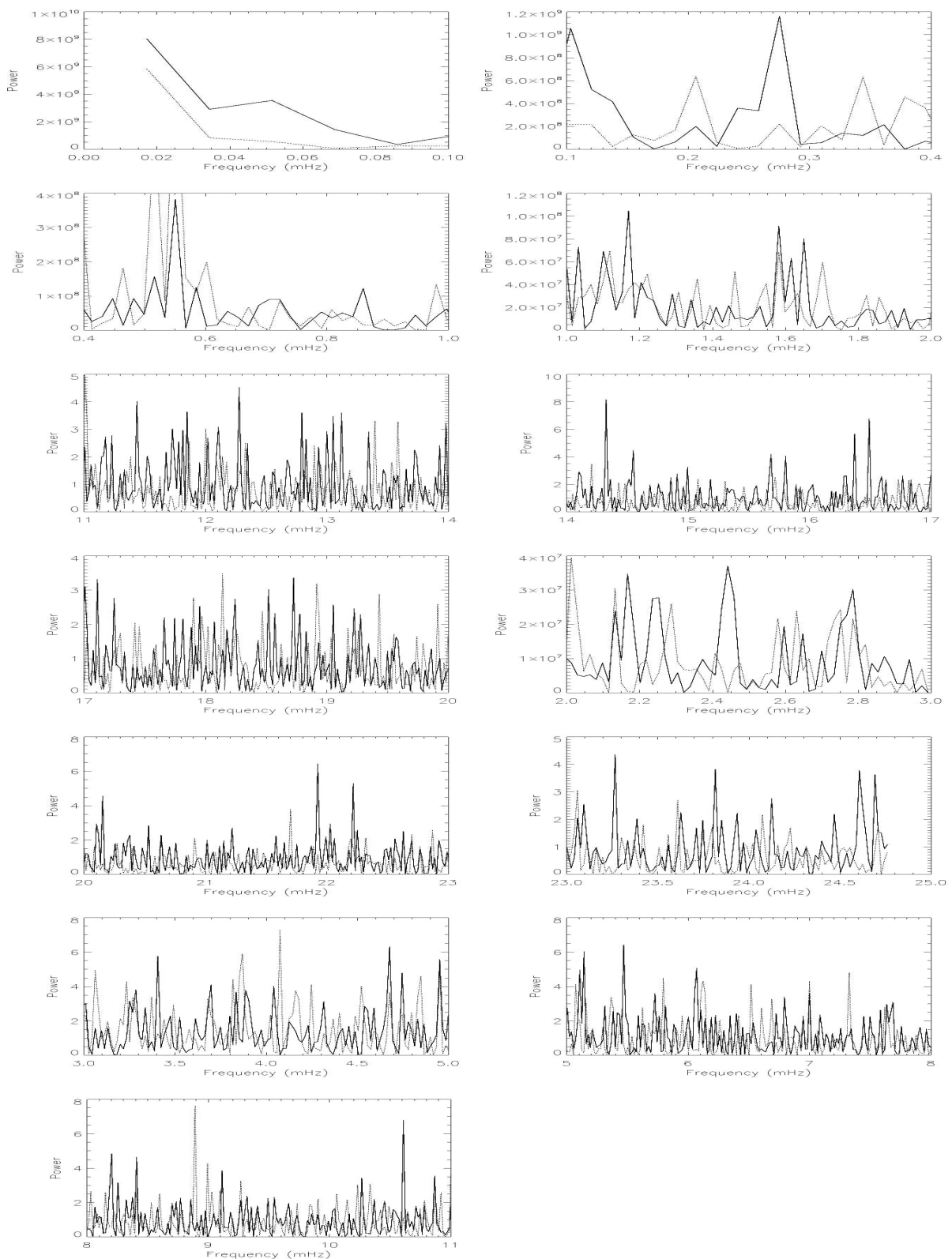


**Fig. A.1.** Filament and reference periodograms for 22 Nov. 2003 (Fil 1). Continuous line: filament; dotted line: reference area.

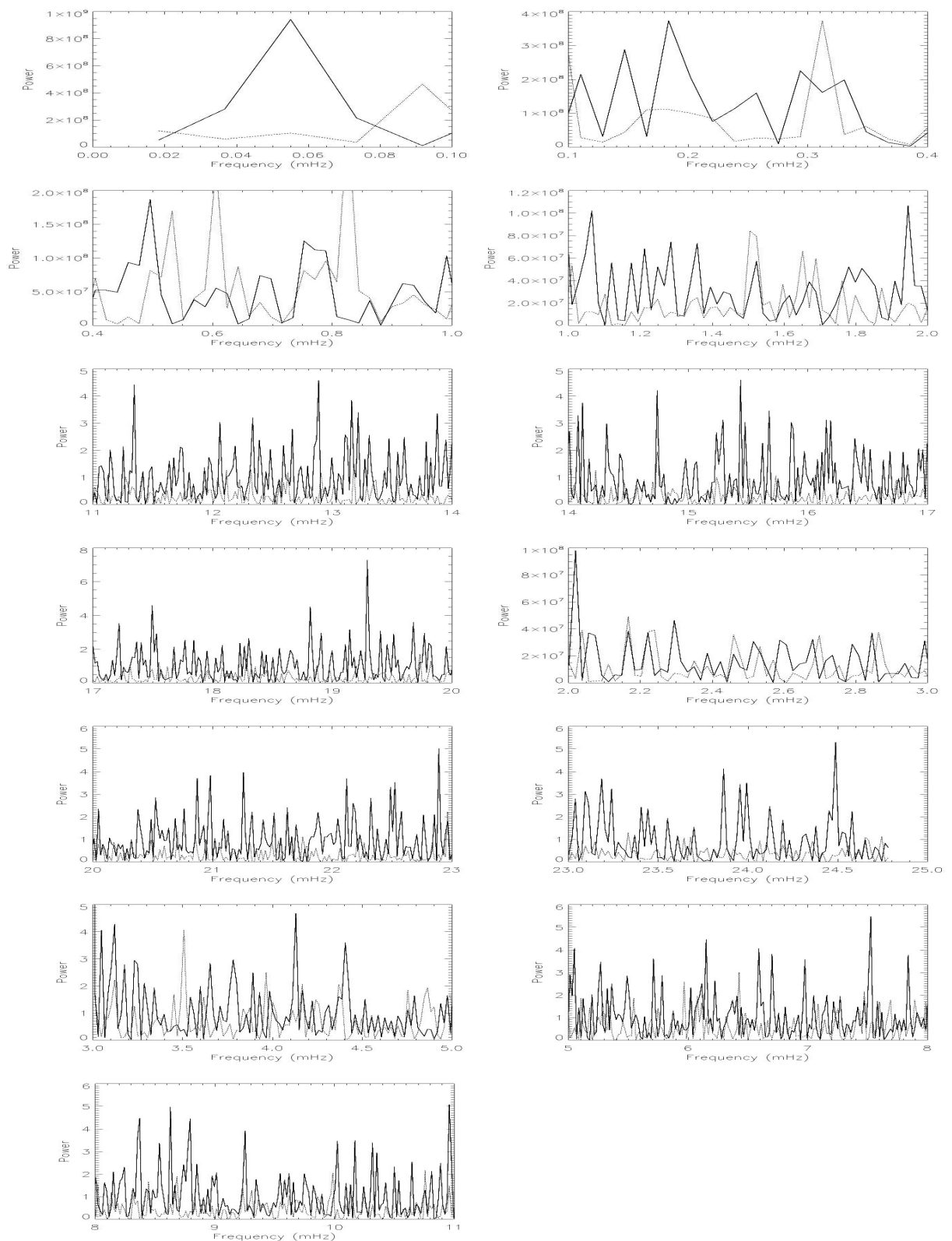


**Fig. A.2.** Filament and reference periodograms for 11 Nov. 2004 (Fil 2). Continuous line: filament; dotted line: reference area.

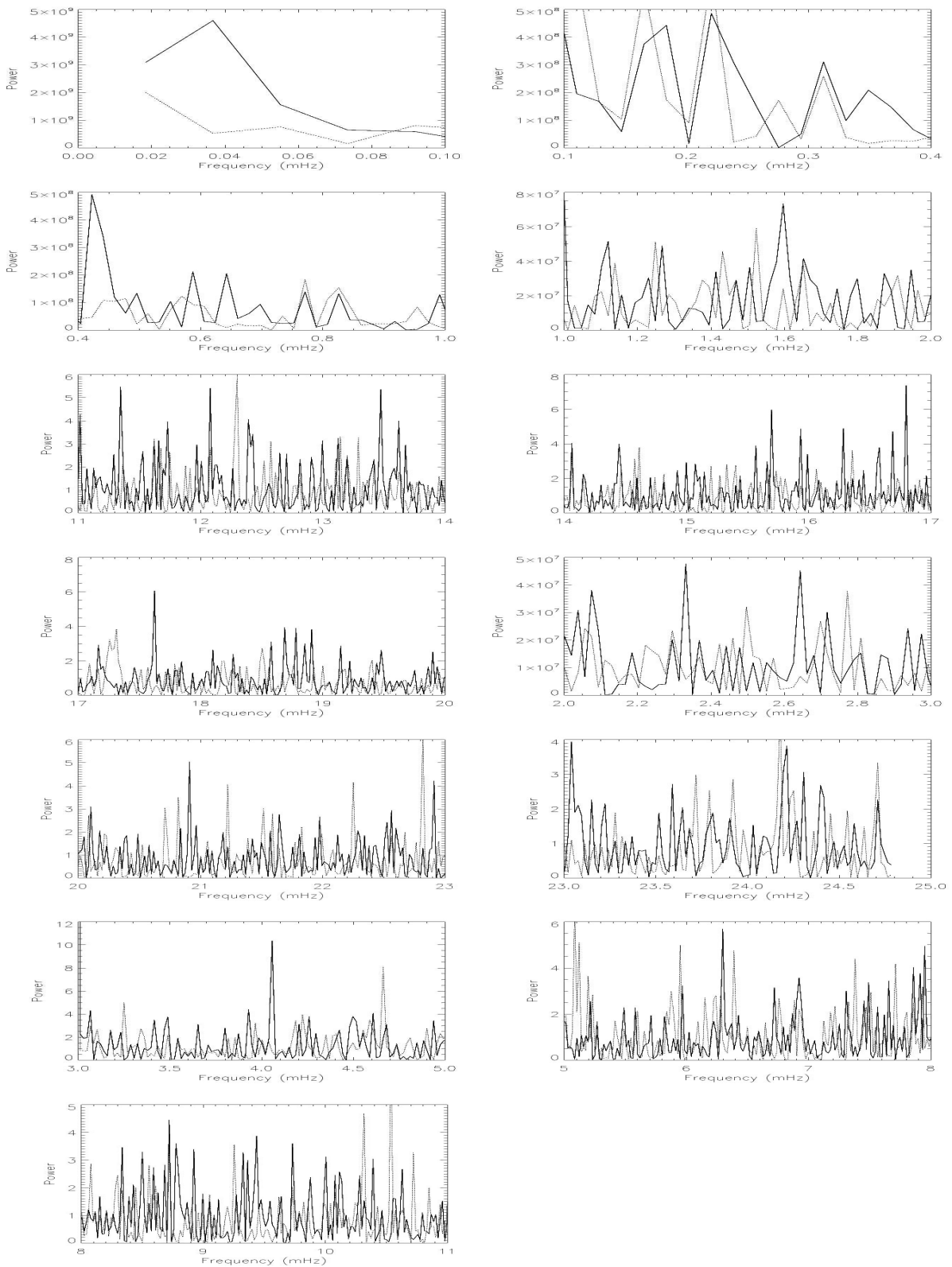


**Fig. A.3.** Filament and reference periodograms for 12 Nov. 2004 (Fil 3). Continuous line: filament; dotted line: reference area.